Available online at www.sciencedirect.com

SciVerse ScienceDirect

Synthesis, studies and fuel cell performance of "core–shell" electrocatalysts for oxygen reduction reaction based on a PtNi$_x$ carbon nitride "shell" and a pyrolyzed polyketone nanoball "core"

V. Di Noto [a,b,*], E. Negro [a,b], S. Polizzi [b,c], K. Vezzù [d], L. Toniolo [b,c], G. Cavinato [a]

[a] Department of Chemical Sciences, University of Padova, Via Marzolo 1, I-35131 Padova (PD), Italy
[b] Consorzio Interuniversitario Nazionale per la Scienza e la Tecnologia dei Materiali, INSTM, Italy
[c] Department of Molecular Sciences and Nanosystems, University of Venice, Calle Larga S. Marta, Dorsoduro, 2137-30123 Venezia (VE), Italy
[d] Veneto Nanotech S.C.p.a., Via San Crispino 106, I-35129 Padova (PD), Italy

ARTICLE INFO

ABSTRACT

This report describes a new class of "core–shell" electrocatalysts for oxygen reduction reaction (ORR) processes for application in Proton Exchange Membrane Fuel Cells (PEMFCs). The electrocatalysts are obtained by supporting a "shell" consisting of PtNi$_x$ alloy nanoparticles embedded into a carbon nitride matrix (indicated as PtNi$_x$-CN) on a "core" of pyrolyzed polyketone nanoballs, labeled 'ST$_p$'. ST$_p$s are obtained by the sulfonation and pyrolysis of a precursor consisting of XC-72R carbon nanoparticles wrapped by polyketone (PK) fibers. The ST$_p$s are extensively characterized in terms of the chemical composition, thermal stability, degree of graphitization and morphology. The "core–shell" ORR electrocatalysts are prepared by the pyrolysis of precursors obtained impregnating the ST$_p$ "cores" with a zeolitic inorganic–organic polymer electrolyte (Z-IOPE) plastic material. The electrochemical performance of the electrocatalysts in the ORR is tested "*in situ*" by single fuel cell tests. The interplay between the chemical composition, the degree of graphitization of both PtNi$_x$-CN "shell" and ST$_p$s "cores", the morphology of the electrocatalysts and the fuel cell performance is elucidated. The most crucial preparation parameters for the optimization of the various features affecting the fuel cell performance of this promising class of ORR electrocatalysts are identified.

* Corresponding author. Department of Chemical Sciences, University of Padova, Via Marzolo 1, I-35131 Padova (PD), Italy. Tel./fax: +39 049 827 5229.
E-mail address: vito.dinoto@unipd.it (V. Di Noto).

1.   Introduction

Fuel cells (FCs) are a family of open electrochemical energy conversion devices operating through the direct electro-oxidation of a fuel (e.g., hydrogen) at the anode and the reduction of an oxidant, usually the oxygen of air, at the cathode [1–3]. Particular attention has been attracted by a family of FCs relying on a proton exchange membrane (PEM) as the electrolyte; these systems are known as proton exchange membrane fuel cells (PEMFCs) [4]. PEMFCs are compact systems characterized by a very high energy conversion efficiency, up to 2–3 times larger in comparison with competing technologies such as internal combustion engines (ICEs) [5]. PEMFCs are particularly suitable to power light-duty electric vehicles and portable electronic devices such as audiovisual players and laptop computers [6,7]. One of the most important bottlenecks in the operation of PEMFCs is the sluggish kinetics of the oxygen reduction reaction (ORR) [8]. Suitable electrocatalysts are required to promote the ORR kinetics in order to achieve an improved performance. As of today, the state of the art in ORR electrocatalysts for PEMFCs consists in nanocomposite materials including platinum nanocrystals supported on active carbons characterized by a large surface area and a high electronic conductivity such as XC-72R carbon black [9,10]. These electrocatalysts afford a satisfactory performance; however, they are also very expensive owing to a significant loading of platinum (usually between 10 and 50 wt %) [11]. Furthermore, they suffer from an insufficient long-term durability [12–14]. These drawbacks are still major obstacles towards a widespread diffusion of the promising PEMFC technology. Several approaches are attempted to address the above issues. On one hand, ORR active sites showing an improved turnover frequency were prepared. In general, they include a platinum-group metal (PGM, e.g., Pt, Pd) [10,15] alloyed with one or more first-row transition metals (e.g., Cr, Fe, Co, Ni, Cu) [16–24]. On the other hand, a variety of new supports were investigated, including carbon nanoparticles, graphene layers, and carbon nanotubes; some of these systems include suitable heteroatoms (e.g., N or S) to stabilize the active sites and improve the activity and durability of the electrocatalysts [25–27]. In the last decade, our research group proposed an innovative protocol to obtain electrocatalysts for application in fuel cells [28,29]. A suitable hybrid inorganic–organic precursor is prepared, consisting of complexes of the desired metal atoms networked by an organic binder. The precursor undergoes a series of pyrolysis and activation steps, yielding the final electrocatalyst; the latter's stoichiometry is well-controlled and includes the desired concentration of heteroatoms (typically N). The obtained carbon nitride-based electrocatalysts present an improved performance and tolerance to oxidizing conditions [29–31]. The best results are reached in the electrocatalysts with a "core–shell" morphology [30,32,33]. In these systems, the hybrid inorganic–organic precursor is used to impregnate a suitable support before the pyrolysis and activation steps. Highly conductive XC-72R carbon nanoparticles (NPs) were adopted. In such "core–shell" morphology an improved dispersion of the active sites embedded in the carbon nitride "shell" was obtained, which resulted in a better fuel cell performance in comparison with the corresponding bulk electrocatalysts including active sites with the same stoichiometry [32].

In this paper, a new family of supports characterized by an innovative morphology and a large surface area is developed. The supports consist of nanoballs of carbon nanofibers with a diameter on the order of nanometers wrapping "core" carbon nanoparticles of ca. 30–50 nm in size. The supports are obtained in two steps: (1) polyketone (PK) fibers are grown on XC-72R carbon NPs acting as nucleation centers, giving so rise to "balls" showing a nanofibrous morphology; thus, the "support precursor" (SP) is obtained [34]; (2) SP undergoes sulfonation and multi-step pyrolysis procedures. The resulting supports are adopted as the "core" in the preparation of advanced "core–shell" ORR carbon nitride electrocatalysts. In these systems, the "core" is covered by a $PtNi_x$-CN "shell" based on $PtNi_x$ alloy NPs embedded in a carbon nitride (CN) matrix. The "balls" with a nanofibrous morphology of SP are proposed as an innovative template for the modulation of: (a) the morphology and chemical composition of the supports; and (b) the activity and selectivity of the "core–shell" carbon nitride electrocatalysts, which are briefly indicated as PtNi-CN_l T_f/ST_p (see the following discussion for more information). PtNi-CN_l T_f/ST_p are studied in terms of composition, morphology and single-cell performance under operating conditions in order to obtain information on the most important preparation parameters to design next-generation ORR electrocatalysts characterized by an improved efficiency.

2.   Experimental

2.1.   Reagents

Potassium tetrachloroplatinate (II), 99.9% and potassium tetracyanonickelate (II), hydrate are supplied by ABCR. D(+)-sucrose, biochemical grade is Acros reagent. EC-20 is received from ElectroChem, Inc. (nominal Pt loading: 20%) and used as the reference. In the following text, EC-20 is labeled "Pt/C reference". Palladium (II) acetate, 98%, p-toluenesulfonic acid monohydrate, 98% and 1,3-bis(diphenylphosphino) propane are obtained from Sigma–Aldrich and in the following are labeled Pd(AcO)$_2$, TsOH, and dppp, respectively. Methanol is purchased by Baker, while sulfuric acid, 98% is obtained from Carlo Erba. All these reagents and solvents are used as received. Carbon monoxide and ethane (C$_2$H$_4$) are supplied by SIAD Company ('research grade', purity > 99.9%). XC-72R carbon black is provided as a courtesy by Carbocrom s.r.l. and washed with H$_2$O$_2$ 10 vol.% prior to use.

2.2.   Synthesis of the samples

2.2.1.   Preparation of the ST_p "core" supports
The [Pd(dppp)(H$_2$O)(TsOH)](TsOH) and PK are prepared as described in the literature [35,36]. The synthesis of PK is carried out under 45 atm of CO and C$_2$H$_4$ (CO/C$_2$H$_4$ = 1/1) at 85 °C using 0.01 mmol of [Pd(dppp)(H$_2$O)(TsOH)](TsOH), 0.1 mmol of TsOH, 80 mL of MeOH and 1.3 mL of water. After 1 h, the yield is of 6.2 g of PK. The support precursor, labeled "SP", is

prepared by carrying out the copolymerization of CO and C_2H_4 in the presence of 530 mg of XC-72R as described above for the production of PK. The yield is of 5.0 g of a coarse, gray powder. A few grams of SP are put into a flask filled with ca. 150 mL of H_2SO_4, 98% and heated at 150 °C under reflux for 45 min. The product is then poured slowly into ca. 500 mL of cold bidistilled water. The obtained black suspension is filtered and copiously washed with bidistilled water until the pH of the filtrate becomes neutral. The resulting material is dried in a ventilated oven for one night at $T = 120$ °C and finely ground into a planetary ball mill. The product is a fine, blackish powder which is labeled "SSP" (Sulfonated Support Precursor). SSP is dried under 10^{-3} mbar of vacuum at 120 °C for 2 h. The resulting product is transferred into a quartz tube, which is connected to a rotary pump establishing a dynamic vacuum of 10^{-3} mbar. The product undergoes a thermal treatment consisting of a first step at 150 °C lasting 7 h and a second step at 300 °C lasting 2 h. The resulting ST_p support is a fine, black powder labeled "S300". An aliquot of S300 undergoes a pyrolysis step at 500 °C for 2 h under dynamic vacuum in the same experimental setup described above, giving so rise to the ST_p support labeled "S500". A second aliquot of S300 undergoes a different pyrolysis process under dynamic vacuum in the same experimental setup described above. The pyrolysis process consists in a first step at 600 °C for 2 h, followed immediately by a second step at 700 °C lasting 2 h. The ST_p support labeled "S700" is thus obtained.

2.2.2. Preparation of the electrocatalysts

The electrocatalysts are prepared according to a protocol described in detail elsewhere [28,32]. 0.482 mmol of K_2PtCl_4 and 0.685 mmol of $K_2Ni(CN)_4$ are each dissolved into ca. 2 mL of bidistilled water, yielding the solutions A and B, respectively. 533 mg (1.56 mmol) of sucrose are dissolved in ca. 2 mL of bidistilled water, resulting in a transparent solution which is equally divided between solution A and solution B. 533 mg of S500 are added to solution B, which is then extensively homogenized with an ultrasonic probe (Bandelin 2200). Solution A is added dropwise to solution B, under stirring. The suspension is vigorously stirred for two days. Water is removed from the obtained gel by a thermal treatment carried out at 120 °C in a ventilated oven, yielding the "catalyst precursor". The catalyst precursor obtained including the S500 ST_p "core" support is labeled "CP500". The whole procedure described above is repeated, with the only difference that S700 is used as the ST_p "core" support and the catalyst precursor labeled "CP700" is obtained. CP500 is inserted into a quartz tube and undergoes the following three-step pyrolysis process under dynamic vacuum (10^{-3} mbar): step 1, $T = 150$ °C for 7 h; step 2, $T = 300$ °C for 2 h; step 3, $T = 600$ °C for 2 h. An aliquot of the resulting product undergoes an additional pyrolysis step at $T = 900$ °C for 2 h under vacuum. The products are labeled PtNi-CN$_l$ T_f/ST_p as reported elsewhere [29]. PtNi-CN$_l$ 600/S500 and PtNi-CN$_l$ 900/S500 are washed three times with bidistilled water and then dried under an IR lamp. For the sake of clarity, in the label T_f is the temperature of the pyrolysis process of the electrocatalyst, while T_p is the temperature of the pyrolysis process of the ST_p "core" support. An aliquot of both PtNi-CN$_l$ 600/S500 and PtNi-CN$_l$ 900/S500 is treated three times with H_2O_2 5% vol. at room temperature and then dried with an IR

lamp, yielding "PtNi-CN$_l$ 600/S500(w)" and "PtNi-CN$_l$ 900/S500(w)", respectively. The protocol described above is also applied to CP700. Thus, four additional products are obtained: (a) PtNi-CN$_l$ 600/S700 and PtNi-CN$_l$ 900/S700 (pristine electrocatalysts); and (b) PtNi-CN$_l$ 600/S700(w) and PtNi-CN$_l$ 900/S700(w) (electrocatalysts treated with H_2O_2).

2.3. Instruments and methods

C, H, N and S are determined via elemental analysis using a FISONS EA-1108 CHNS-O instrument. The concentration of metals in the electrocatalysts is evaluated by inductively coupled plasma atomic emission spectroscopy (ICP-AES), adopting the method of standard additions. The following emission lines are considered: λ(Pt) = 214.423 nm; λ(Ni) = 231.604 nm; and λ(K) = 766.490 nm. Measurements are collected with a Spectroflame Modula sequential and simultaneous ICP-AES spectrometer equipped with a capillary cross-flow nebulizer (Spectroanalytical, Kleve, Germany). Analytical determinations are carried out using a plasma power of 1.2 kW, a radio frequency generator of 27.12 MHz, and an argon gas flow with nebulizer, auxiliary and coolant set at 1, 0.5 and 14 L min^{-1}, respectively. The samples are mineralized as described elsewhere [15]. A High-Res modulated TGA 2950 thermogravimetric analyzer, produced by TA instruments, is used to carry out the thermal analyses. An open platinum pan is used; the temperature range between 30 and 1000 °C is explored. The samples are analyzed both in N_2 and in oxidizing air atmosphere. N_2 adsorption measurements are carried out at 77 K using a Quantachrome Nova 1200e Surface Area and Pore Analyzer. The surface area of the samples is evaluated by means of multi-point Brunauer−Emmet−Teller (BET) method (in the range 0.02−0.3 p/p_0), while the micropore area is derived with the de Boer statistical thickness method in the range from 0.2 to 0.5 p/p_0. FT-IR measurements in mid-IR are executed with a Nicolet FT-IR Nexus spectrometer, at a resolution of 4 cm^{-1}. The instrument mounts a DTGS (deuterated triglycine sulfate) KBr detector and a KBr beam splitter to acquire measurements. FT-MIR measurements are derived by averaging 500 scans obtained with the DRIFT (Diffuse Reflectance Infrared Fourier Transform) accessory over the pristine samples. Baseline correction is carried out with Nicolet FT-IR Nexus spectrometer software. μ-Raman spectra are determined on a homemade instrument described elsewhere [37]. HR-TEM analysis is executed at 300 kV using a Jeol 3010 apparatus with a high-resolution pole piece (0.17 nm point-to-point resolution), equipped with a Gatan slowscan 794 CCD camera. The samples for HR-TEM inspection are prepared as described elsewhere [38].

2.4. Fabrication of membrane−electrode assemblies (MEAs) and tests in a single fuel cell

The MEAs are prepared with a catalyst-coated substrate procedure as described elsewhere [39]. EC-20 is used as the anode electrocatalyst and commercial Nafion117™[1] membranes (Ion

---

[1] The DuPont Oval Logo, DuPont™, The miracles of science™ and all products denoted with a ™ and ® are trademarks or registered trademarks of DuPont or its affiliates."
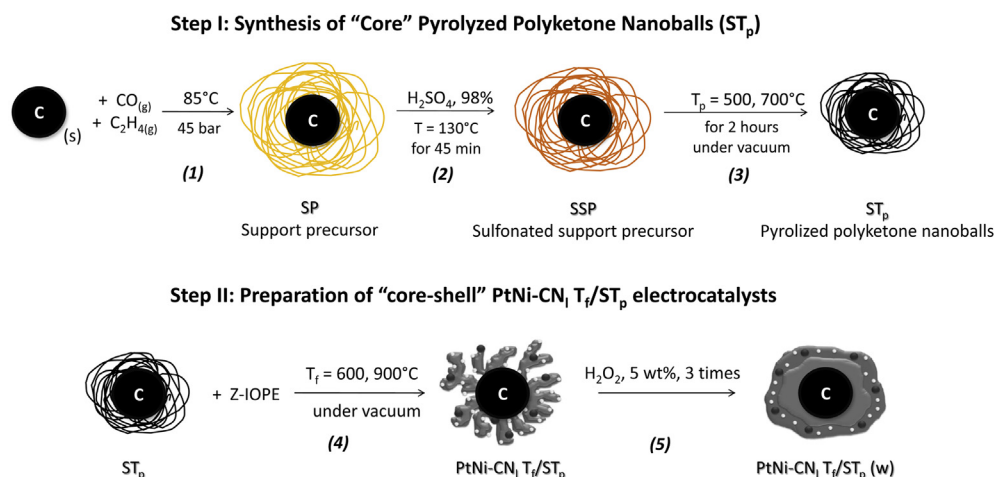
Power) are adopted as the membrane. The platinum loadings in the anodic and the cathodic electrocatalytic layers are 0.4 and 0.1 mg cm^{-2}, respectively. The Nafion/C ratio is 0.6. All of the cathode electrocatalysts are dispersed with XC-72R in a 1:1 weight ratio. The electrocatalytic layers are deposited on GDS1120 carbon paper (Ballard Material Products). The resulting gas diffusion electrodes (GDEs) are hot-pressed onto the membranes as previously described [30]. Single fuel cell tests are executed as described elsewhere using a back pressure of the reagents equal to either 4 bar and 1 bar [40].

3. Results and discussion

3.1. Preparation observations

The proposed electrocatalysts are prepared in two steps, I and II, as shown in Scheme 1. In step I, the electron-conducting "core" (ST_p) is prepared, which is characterized by a high surface area. In detail, ST_p is synthesized as follows. First, the support precursor (SP) is obtained by copolymerization of CO with ethene in the presence of XC-72R carbon NPs suspended in a methanol/water solution (see the Experimental section). In this process the carbon NPs, which adsorb the polymerization catalysts, act as nucleation centers for the polymerization of PK fibers. Before the pyrolysis process the SP nanoparticles, which consist of "nanoballs" of PK fibers embedding XC-72R carbon NPs, are made infusible by a treatment with conc. H_2SO_4. This last treatment transforms SP into the infusible sulfonated support precursor (SSP). The desired "core" nanoparticles for the final electrocatalysts are obtained by pyrolysis at $T_p = 500$ and 700 °C for 2 h under vacuum of SSP (see the Experimental section for the details). This process gives rise to highly electron-conducting nanoparticles, characterized by a large and rough surface area owing to the "qualis pater, talis filius" morphological phenomenon of replication, yielding ST_ps. In step II, the Z-IOPE (Zeolitic Inorganic–Organic Polymer Electrolyte) precursor, widely described elsewhere [29,37,41–43], which consists of cluster aggregates of Pt and Ni complexes bridged together by sucrose molecules, is adsorbed on the surface of the obtained ST_p "core" nanoparticles. The pyrolysis at $T_f = 600$ and 900 °C (step 4 of Scheme 1) of these latter precursors allows us to obtain the desired electrocatalysts, labeled PtNi-CN$_l$ T_f/ST_p. The label indicates that the "shell", PtNi-CN$_l$ T_f, is based on PtNi alloy nanoparticles embedded in a CN "shell" matrix with a nitrogen concentration lower than 5%, which was obtained at T_f./ST_p indicates that the "shell" described above is supported on a "core" of ST_p, which is prepared as previously discussed. The general procedure adopted for the preparation of electrocatalysts with a CN "shell" covering a conductive "core" may include a treatment in H_2O_2 [28]. This step was originally introduced with the following purposes: (a) to remove the contaminants from the active sites; and (b) to help bringing the co-catalysts included in the active sites (in general, first-row transition metals such as Fe, Co and Ni) to their oxidized state, to improve the performance in the ORR of the electrocatalyst according to a mechanism proposed elsewhere [29,38]. In this work, the supports used as the "core" are completely different with respect to those adopted in our previous research, in terms of both morphology and chemical composition [29]. In particular, a much rougher morphology was expected in comparison with other "core–shell" systems, possibly hindering the mass transport of reagents and products to the active sites. Furthermore, the sulfur atoms present in the supports could coordinate strongly the PtNi alloy nanoparticles bearing the active sites, reducing their performance in the ORR. Consequently, to address these issues and achieve a good activation of the electrocatalysts, the treatment in H_2O_2 applied to the proposed PtNi-CN$_l$ T_f/ST_p materials is more extensive with respect to that described elsewhere [28,29], and it consists of three steps in H_2O_2 5% vol. as described in the Experimental section; it yields the materials labeled PtNi-CN$_l$ T_f/ST_p(w). The latter are studied in detail to elucidate the effects of the treatment in H_2O_2 on critical features of the electrocatalysts such as the chemical composition, the morphology and the electrochemical performance. The stoichiometry of all the prepared materials is briefly summarized in Tables 1 and 2.

Step I: Synthesis of "Core" Pyrolyzed Polyketone Nanoballs (ST_p)

Step II: Preparation of "core-shell" PtNi-CN$_l$ T_f/ST_p electrocatalysts

Scheme 1 – Preparation procedure of pyrolyzed polyketone nanoballs (ST_p), and of PtNi-CN$_l$ T_f/ST_p and PtNi-CN$_l$ T_f/ST_p(w) "core–shell" electrocatalysts.

Table 1 – Chemical composition of the ST_p supports and of their precursors.

Material[a]	Weight%			Formula
	C[b]	H[b]	S[b]	
SP	66.17	6.76	–	$CH_{1.22}$
SSP	57.21	2.48	6.51	$CH_{0.52}S_{0.043}$
S300	65.79	2.12	4.20	$CH_{0.38}S_{0.024}$
S500	81.48	1.55	1.99	$CH_{0.23}S_{0.0092}$
S700	76.91	1.63	2.59	$CH_{0.25}S_{0.013}$
Pristine PK	64.38	7.27	–	C_3H_4O

[a] SP = support precursor; SSP = sulfonated support precursor; S300, S500 and S700 = ST_p supports.
[b] By elemental analysis.

3.2. Stoichiometry of ST_p "core" supports and PtNi-CN$_l$ T_f/ST_p electrocatalysts

3.2.1. ST_p "core" supports

The chemical composition of SP (see Table 1) is coherent with a composite material including ca. 6 wt% of carbon, while the remaining fraction consists of a polymer with the same stoichiometry as pristine PK. Thus, it can be assumed that SP consists of $-(-CH_2CH_2C=O)_n-$ PK fibers grown on XC-72R carbon NP "cores". SSP includes 6.51 wt% of sulfur; this evidence is interpreted admitting that the treatment in conc. H_2SO_4 results in the functionalization of the PK fibers of SP with sulfur-based groups such as $-SO_3H$ and others. Thus, in SSP ca. 14% of the PK repeating units are functionalized by sulfur-based groups. In addition, the wt% of hydrogen in SP decreases by ca. 2/3 upon treatment with conc. H_2SO_4 owing to its strong dehydrating effect. In S300 a lower concentration of sulfur and hydrogen is detected with respect to SSP as a result of the removal of volatile species containing hydrogen and sulfur by pyrolysis. S500 and S700 show similar compositions, and are characterized by: (a) a high concentration of carbon, up to over 80 wt%; and (b) a concentration of hydrogen and sulfur equal to ca. 1.6 and 2.3 wt%, respectively (see Table 1).

Results show that after the pyrolysis process the graphitization of both S500 and S700 ST_p supports is essentially complete. The increase in C from ca. 65 wt% in S300 to ca. 80% in both S500 and S700 is ascribed to an almost complete thermal elimination of oxygen-containing species from the materials. A small amount of H and S is still detected in both S500 and S700, thus witnessing that the S atoms are embedded in the graphitic layers, while the H atoms are located at their edges.

3.2.2. PtNi-CN$_l$ T_f/ST_p electrocatalysts

The chemical composition of the electrocatalysts is determined by ICP-AES spectroscopy and elemental analysis. The results are summarized in Table 2. The PtNi-CN$_l$ T_f/ST_p electrocatalysts show a Pt:Ni atomic ratio close to the expected value of 1/1, which is in accordance with results described elsewhere from similar electrocatalysts [30] and is a further proof of the good control of the metal composition achieved in materials by the proposed preparation route [28,29]. PtNi-CN$_l$ T_f/ST_p include a small wt% of potassium despite extensive washing procedures, which counterbalances the negative charge present on anionic metal coordination species whose metal centers do not undergo reduction during the pyrolysis processes [29]. The advancement on T_f in the graphitization process of the PtNi$_x$-CN "shell" of electrocatalysts (see Table 2) is witnessed by: (a) the decrease in the concentration of hydrogen and nitrogen; and (b) the increase in the concentration of sulfur. The results for sulfur atoms are expected if we consider that the latter specie is provided by the S500 and S700 ST_p "core" supports and that the PtNi$_x$-CN "shell" is covering the S500 and S700 ST_p "core" supports [32]. The PtNi$_x$-CN "shell" inhibits the removal of sulfur-based volatile species present in the ST_p "core" supports during the pyrolysis process. In summary, while the overall PtNi$_x$-CN "shell" of the electrocatalysts is progressively graphitized as T_f is raised, the sulfur atoms in the ST_p "core" support are kept constant (see Table 2). The concentrations of metal atoms and sulfur increase in the order: PtNi-CN$_l$ T_f/S500 < PtNi-CN$_l$ T_f/S700. The thermal elimination of volatile species occurs more easily in samples supported on S500 with respect to those supported on

Table 2 – Composition of the materials.

Electrocatalyst	Weight%							Formula
	K[a]	Pt[a]	Ni[a]	C[b]	H[b]	N[b]	S[b]	
a) Pristine electrocatalysts								
PtNi-CN$_l$ 600/S500	0.40	9.3	3.1	59.9	0.84	1.25	0.98	$K_{0.22}[PtNi_{1.11}C_{104}H_{17.4}N_{1.87}S_{0.64}]$
PtNi-CN$_l$ 900/S500	0.33	11.8	4.6	81.9	0.22	1.06	1.88	$K_{0.14}[PtNi_{1.29}C_{113}H_{3.6}N_{1.25}S_{0.97}]$
PtNi-CN$_l$ 600/S700	0.58	16.7	6.1	63.9	0.85	1.33	3.12	$K_{0.17}[PtNi_{1.21}C_{62}H_{9.9}N_{1.11}S_{1.14}]$
PtNi-CN$_l$ 900/S700	0.35	15.0	4.3	71.7	0.33	0.93	3.69	$K_{0.12}[PtNi_{0.94}C_{78}H_{4.3}N_{0.86}S_{1.50}]$
b) Electrocatalysts after treatment with H_2O_2								
PtNi-CN$_l$ 600/S500(w)	0.30	3.5	0.8	69.1	1.28	1.46	1.13	$K_{0.42}[PtNi_{0.76}C_{323}H_{71.3}N_{5.6}S_{2.0}]$
PtNi-CN$_l$ 900/S500(w)	1.1	15.7	5.8	68.6	0.49	0.60	1.36	$K_{0.35}[PtNi_{1.24}C_{71}H_{6.1}N_{0.5}S_{0.5}]$
PtNi-CN$_l$ 600/S700(w)	0.48	14.8	5.2	57.1	0.92	0.99	0.85	$K_{0.16}[PtNi_{1.16}C_{62}H_{12}N_{0.9}S_{0.3}]$
PtNi-CN$_l$ 900/S700(w)	0.33	22.2	8.5	63.1	0.32	0.68	2.50	$K_{0.07}[PtNi_{1.28}C_{46}H_{2.8}N_{0.4}S_{0.7}]$
Pt/C reference[c]		20.0		80.0				$[PtC_{65}]$

[a] Determined by ICP-AES spectroscopy.
[b] By elemental analysis.
[c] Nominal values.

S700. The treatment of the electrocatalysts with H_2O_2 gives rise to the following effects: (a) at $T_f = 600\ °C$ the metal concentration is reduced, while the reverse trend is observed at $T_f = 900\ °C$; and (b) the concentrations of N and S are decreased. This evidence is interpreted admitting that H_2O_2 attacks preferentially the defects on the PtNi$_x$-CN "shells" of the PtNi-CN$_l$ T_f/ST$_p$ electrocatalysts. At $T_f = 600\ °C$, N and S heteroatoms are removed upon treatment with H_2O_2 and the graphitization of the CN "shell" matrix is not complete. As a consequence, it is expected that: (a) the CN "shell" matrix is highly susceptible to oxidative degradation; and (b) in PtNi-CN$_l$ T_f/ST$_p$, PtNi$_x$ alloy NPs are removed after the treatment with H_2O_2. This behavior is easily explained if we consider that PtNi$_x$ alloy NPs, which are fixed in the N-based coordination "nests" in the CN "shell" [44], are easily released after the elimination of N atoms upon the treatment with H_2O_2. At $T_f = 900\ °C$, the graphitization of the CN "shell" matrix is essentially complete, thus it is more difficult to remove by treatment with H_2O_2 the N and S heteroatoms embedded in the CN "shell" matrix and in the ST$_p$ "core" support, respectively. Consequently, after a partial oxidation of the support matrices, the metal concentration increases (see Table 2).

3.3. Investigations on ST$_p$ "core" supports

3.3.1. HR-TGA analysis

The TG profiles of the ST$_p$ "core" supports and their precursors under oxidizing and inert atmospheres are reported in Fig. 1. A single decomposition event is evidenced for XC-72R carbon NPs at ca. 650 °C in an oxidizing atmosphere. The small mass loss of less than 2 wt% at $T = 100\ °C$ is ascribed to the desorption from the sample of atmospheric moisture. The TG profile under oxidizing atmosphere of the samples is complex, indeed: (a) a mass loss lower than ca. 10% is evidenced at $T \leq 100\ °C$; (b) 70–80% of the initial mass of the sample is lost at $400 < T < 500\ °C$; and (c) the residue undergoes oxidation at $650 < T < 750\ °C$. The mass loss observed at low temperature, attributed to the desorption of atmospheric moisture from the samples, is diagnostic of the hygroscopic character of materials which decreases in the order: SSP > S300 ~ S700 > S500 ~ XC-72R > SP. This trend matches closely the concentration of sulfur in the materials (see Table 1). Thus, sulfur atoms give rise to hygroscopic surface functional groups, which play a crucial role in the ability of the materials to adsorb the moisture. No sulfur is present in SP, which shows a very small mass loss at low temperature and no significant thermal degradation up to ca. 300 °C. Thus, the thermal stability of the PK fibers is remarkable. It is likely that PK provides up to 90 wt% or more of the mass eliminated by SP (see Section 3.2.1.). The thermal stability of the here described materials in oxidizing atmosphere ranges from 400° to 500 °C and increases in the order: SSP < SP ~ S300 < S700 < S500 < XC-72R. This order is in agreement with the graphitization degree of the samples as T_p is raised. A thermal stability of SP higher than that of SSP is interpreted admitting that the treatment with conc. H_2SO_4 eliminates the oxygen-based keto groups of SP, reducing the density of interchain dipole–dipole interactions. In oxidizing atmosphere, the mass loss of samples from 500° to 650 °C is relatively limited and the residue increases from ca. 7 to
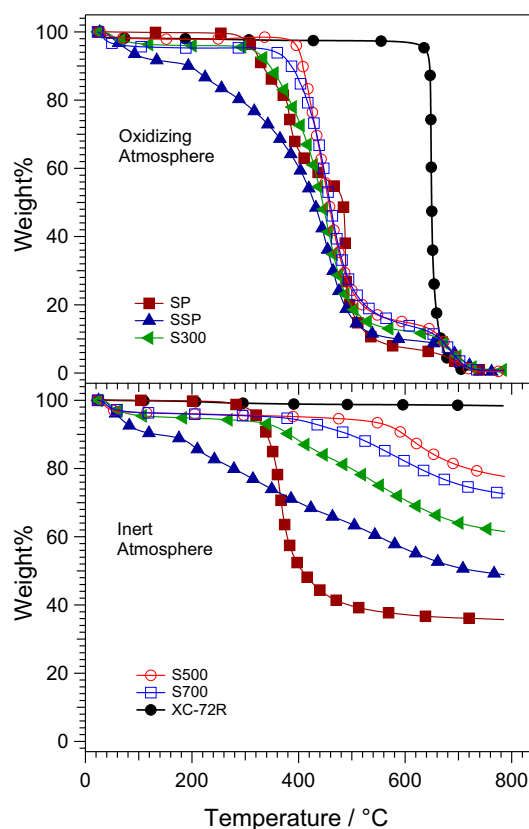

Fig. 1 – TG profiles of the ST$_p$ "core" supports and their precursors under oxidizing atmosphere (upper panel) and under inert atmosphere (lower panel).

15 wt% in the order: SP < SSP < S300 < S500 ~ S700. At $T > 650\ °C$ the TG profiles of the materials are almost coincident, confirming that they are characterized by a "core–shell" morphology where the "shell" consists of a random agglomeration of carbon fibers obtained by pyrolyzing the PK fibers and the "core" XC-72R carbon NPs. It is expected that the thermal stability of the random agglomeration of carbon fibers of the "shells" is inferior in comparison with that of the "cores", as witnessed by the negligible mass loss of XC-72R at $T < 650\ °C$ under an oxidizing atmosphere (see Fig. 1). Therefore, it is hypothesized that the "shells" undergo an almost complete pyrolysis process at $T < 500\ °C$, while from 500 to 650 °C the residues consist mostly of the "core" of XC-72R carbon NPs (see the data of XC-72R in Fig. 1). The amounts of carbon in the materials range from ca. 7% for SP (the expected value is 6%, see Section 3.2.1.), and increase up to ca. 15% for S500 and S700, concurrently with the progressive mass loss of the samples (see Section 2.2.1.). The TG profiles collected under inert atmosphere (lower panel of Fig. 1) are consistent with the TG investigations carried out under oxidizing atmosphere. It is observed that: (a) XC-72R carbon NPs do not undergo any appreciable mass loss up to 800 °C; and (b) the mass losses of the materials at $T = 100\ °C$ match quite closely those measured under an oxidizing atmosphere. In comparison with the results determined under oxidizing atmosphere, the mass losses occurring under inert

atmosphere take place over a significantly broader temperature interval. The only exception is SP, where a mass loss of ca. 60 wt% takes place in a relatively narrow temperature range centered at ca. 370 °C. The variability in the breadths of the temperature intervals of the thermal degradation events described above are explained as follows. As the temperature reaches a certain threshold (ca. 350 °C), in SP the PK fibers of the "shell" undergo a sudden degradation with the elimination of hydrogen-, oxygen- and carbon-based volatile species. SSP has undergone a treatment in conc. H_2SO_4, leading to the concatenation of PK chains by elimination of water, which makes SSP relatively stable under inert atmosphere. It is hypothesized that the graphitization of PK fibers consists in the formation of different types of crosslinking bridges between different PK chains, resulting in the observed broadening of the thermal degradation event. This effect is not as evident under an oxidizing atmosphere (see the upper panel of Fig. 1) as the crosslinked graphitized polymer is easily degraded by the oxygen brought by the gas flow.

3.3.2. FT-IR DRIFT studies
The FT-IR DRIFT spectra of pristine PK, support precursors and ST_p supports are shown in Fig. 2 and their correlative assignment is summarized in Table 3. The vibrational spectra of pristine PK and SP are almost coincident and correspond to vibrational modes typically expected for PK repeating units $-(CH_2CH_2C=O)-$. A detailed analysis of the spectra allows to conclude that: (a) the proposed preparation procedure yields PK materials; and (b) in SP, the influence of the XC-72R carbon NPs on the structure of the PK component is negligible. A
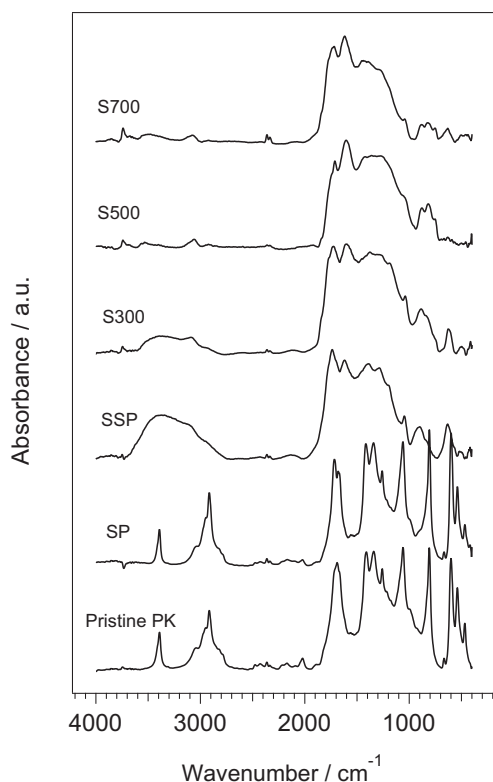

Fig. 2 – FT-IR spectra of pristine PK, support precursors and ST_p supports.

small difference between the spectra of pristine PK and SP lies in the fine details of the region between 1716 and 1668 cm^{-1}, which corresponds to the vibrational modes associated with the stretching of the C=O groups along PK chains [45]. This difference is ascribed to a slightly different composition of PK chains [45]. The spectra of PK and SP also show some features which are ascribed to the terminal groups of the PK chains, which consist of ketone or ester groups [46]. The treatment of SP with conc. H_2SO_4 gives rise to evident structural alterations, as witnessed by the comparison of the spectra of SP and SSP: (a) the sharp peak at 3390 cm^{-1} and the bundle of peaks centered at 2914 cm^{-1} are much broader and more intense; (b) a new shoulder appears at ca. 3120 cm^{-1}; (c) a new peak appears at ca. 1620 cm^{-1}; (d) a broad band appears at ca. 1390 cm^{-1}; (e) the sharp peaks at 1410, 1338 and 1259 cm^{-1} disappear and are substituted by fewer, much broader and less-defined features; (f) the strong and sharp peaks at 1059, 808 and 600 cm^{-1} disappear almost completely and different weaker and broader intensities are detected instead. These behaviors are rationalized admitting that in SSP the treatment with conc. H_2SO_4 yields a condensation process between PK chains with the formation of heteroaromatic rings. Indeed, the various modes attributed to stretching, deformation, bending, wagging and rocking modes of $-CH_2CH_2-$ groups in SP are observed at 2900–2950, 1416, 1342, 1259, 1061 and 808 cm^{-1}, respectively. In SSP these vibrational modes do not present detectable intensities [45,47], while new bands are revealed at 1620, 1460, 1390 and 840 cm^{-1}, which are ascribed to typical IR modes of aromatic graphitic-like systems [44]. Furthermore, SSP shows a band at ca. 3120 cm^{-1} which is attributed to the stretching modes of hydrogen atoms bound to unsaturated carbons [45]. The broadness of the observed IR intensities is consistent with a significant structural disorder in SSP (see Fig. 2). Vibrational modes of several oxygen-containing functional groups are observed in SSP, as witnessed by the bands detected at 1735, 1284, 1047 and 630 cm^{-1} and assigned to $\nu(C=O)$, ether $\nu(C-O)$, alcoholic $\nu(C-O)$ and in-plane $\delta(C=O)$ modes, respectively [44,45,47]. The $\nu(C-O)$ of ether and alcoholic functional groups are located on surface defects of SSP [44]. The introduction of S-based functional groups is confirmed by the band at 1198 cm^{-1}, ascribed to the $\nu_s(SO_2)$ mode. The presence of O- and S-based groups on a highly inhomogeneous conjugated graphitic-like structure is expected to give rise to a highly hydrophilic PK-based material. The broad band detected in SSP at ca. 3370 cm^{-1} is ascribed to $\nu(OH)$ modes of hydroxyl groups involved in hydrogen bonding interactions [45]. The FT-IR spectra of SSP, S300, S500 and S700 show some similarities (see Fig. 2), which are mainly related to the graphitization processes of PK chains resulting after the chemical or thermal treatments of SP. As T_p increases in the order SSP < S300 < S500 < S700, it is observed that: (a) the intensity of the bands ascribed to O- and S-based functional groups becomes progressively weaker; and (b) two peaks, located at ca. 880 and 820 cm^{-1} and assigned respectively to the "breathing" modes of heterocyclic rings and to the out-of-plane A_{2u} graphitic mode, become more and more intense [44]. These evidences are interpreted admitting that the 3D condensation of PK chains forming graphitic-like structures increases the crystallinity of the ST_p supports as T_p is raised. In addition, on T_p: (a) the concentration of SO_x

Table 3 – FT-MIR band assignments of pristine PK, support precursors and ST_p supports.

Pristine PK[a]	SP[a]	SSP[a]	S300[a]	S500[a]	S700[a]	Band assignment[b]	Reference
			3745 (vw)	3741 (vw)	3741 (vw)	ν(OH) water[c]	[45]
3390 (m)	3390 (m)	3373 (m, b)	3369 (w)			ν(OH)[d]	[45]
		3120 (m, sh)	3087 (w)	3065 (vw)	3074 (vw)	Aromatic ν(CH)	[45]
2948 (m, sh)	2947 (m, sh)					ν(CH)$_{as}$	[45]
2914 (s)	2914 (s)	2948 (w, sh)	2931 (vw, sh)			ν(CH)$_{sy}$	[45]
		1735 (vs)	1728 (vs)	1713 (vs)	1726 (vs)	ν(C=O)	[45]
1713 (vs, sh)	1716 (vs)					ν(C=O) ester termination	[46]
1691 (vs)	1679 (s)					ν(C=O)	[45]
1668 (vs, sh)	1668 (s, sh)					ν(C=O)	[45]
		1620 (vs)	1600 (vs)	1600 (vs)	1618 (vs)	G-band in-plane stretching E$_{2u}$	[44]
		1460 (s, sh)	1450 (s, sh)	1425 (s, b)	1442 (s)	A$_{2u}$	[44]
1410 (vs)	1416 (vs)					(CH$_2$) deformation	[47]
		1390 (s)	1375 (vs)	1363 (s, b)	1390 (s, b)	D-band, A$_{1g}$ longitudinal acoustic wave	[44]
1338 (vs)	1342 (vs)					δ(CH$_2$) in-plane	[47]
		1284 (s)	1275 (vs)	1247 (s, b)	1270 (s, b)	ν(C—O) ether	[44]
1259 (s)	1259 (s)					δ(CH$_2$)	[45]
		1198 (s, sh)	1191 (s)	1176 (s, sh)	1182 (m, sh)	ν_s(SO$_2$)	[45]
1059 (vs)	1061 (vs)					ω(CH$_2$)	[47]
		1047 (m)	1037 (m)	1041 (m, sh)	1041 (w, sh)	ν(C—O) alcoholic	[45]
		905 (w)	885 (m)	879 (m)	879 (w)	Heterocyclic ring "breathing"	[44]
		840 (w, sh)	831 (m, sh)	818 (m)	818 (w)	A$_{2u}$ (oop)	[44]
808 (vs)	808 (vs)					ρ(CH$_2$)	[47]
			748 (w, sh)	752 (w)	752 (w)	Graphite-like sp^2 domains	[44]
600 (vs)	598 (vs)	630 (w)	625 (w)	628 (w, b)	628 (w)	δ(C=O) in-plane	[47]
538 (s)	538 (s)					δ(CC=O)	[53]
469 (m)	467 (m)					δ(CCC)	[45]

[a] Relative intensities are reported in parentheses: vs: very strong; s: strong; m: medium; w: weak; vw: very weak; sh: shoulder; b: broad.
[b] ν: stretching; δ: bending; ω: wagging; ρ: rocking; oop: out-of-plane; hy: hydrogen bond.
[c] Stretching vibration of traces of OH groups not involved in hydrogen bonding interactions.
[d] Stretching vibrations of OH groups involved in hydrogen bonding networks.

functional groups decreases, and S atoms are progressively incorporated in the 3D graphitic-like nanodomains; (b) the amount of O-based groups decreases, leading to samples characterized by more hydrophobic surfaces. This result is consistent with the decrease in the amount of water adsorbed on the surface of the samples, revealed by the decrease of the intensity of the band centered at 3370 cm^{-1}.

3.3.3.   μ-Raman investigations

The μ-Raman spectra of XC-72R, of the support precursors and of the ST$_p$ supports are shown in Fig. 3. The μ-Raman profiles show the spectral features typical of graphitic-like materials [48]. SP yields a μ-Raman spectrum similar to that shown by other samples, thus demonstrating that the μ-Raman effect is mainly originated by the "core" XC-72R carbon NPs, on which the PK fibers of SP are grown. The semiquantitative analysis of μ-Raman spectra is carried out by decomposition with Gaussian functions of the spectral features shown in Fig. 3. The very weak broad peak at ca. 1090 cm^{-1} in XC-72R is attributed to ν(CO) stretching modes of oxygenated surface functional groups [32,44]. Two intense modes are identified between 1358 and 1590 cm^{-1} in the materials:

a) the peak at 1358 cm^{-1} is ascribed to the A$_{1g}$ mode of 3D graphitic-like lattice vibrations (D band). In a perfectly ordered 3D infinite graphitic-like lattice, this mode is Raman-inactive [48] and becomes Raman-active owing to

the structural disorder. For instance, the latter may be originated from: (I) the finite dimensions of the ordered domains of the graphitic-like nanoparticles; and (II) the substitution in graphitic materials, during the preparation process, of carbon atoms with heteroatoms (e.g., sulfur, nitrogen) [31,38].
b) the peak at 1590 cm^{-1} is attributed to the E$_{2g}$ graphitic band (G band) [31,38].

The relative intensities of the D and G modes depend on the preparation parameters of samples, such as the growth of PK fibers, the chemical treatment with conc. H$_2$SO$_4$, and T$_p$ values. The ratio between the peak areas under the D and G bands (the I$_D$/I$_G$ ratio) may be used as a figure of merit to gauge the structural disorder of a graphitic sample [31,32]; indeed, as described elsewhere, the I$_D$/I$_G$ ratio increases as the structural disorder of the material rises [49]. Thus, the I$_D$/I$_G$ ratio is correlated to the size of the ordered domains of graphitic samples d$_{dom}$ [44,48]. The decompositions of the μ-Raman spectra shown in Fig. 3 are used to evaluate d$_{dom}$ for the investigated samples. The results are shown in Fig. 4. d$_{dom}$ values decrease from pristine XC-72R to SP (see Fig. 4). Thus, the size of the crystalline domains of XC-72R carbon NPs is reduced as PK fibers are grown; such a reduction in d$_{dom}$ can be rationalized considering that the catalyst for the polymerization of PK is adsorbed on the surface of XC-72R carbon NPs before the preparation of SP and that the growth of PK fibers
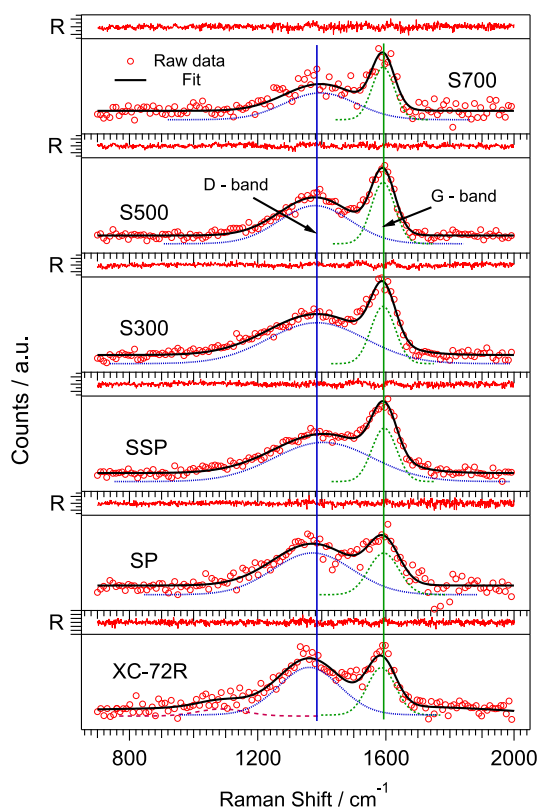
Fig. 3 — Peak decomposition by Gaussian functions of the μ-Raman spectra of the support precursors and ST_p supports. XC-72R is the reference. R refers to the residuals.

starts on their surface, reducing the crystallinity of the outer "layer" of the XC-72R carbon NPs. The treatment of SP in conc. H_2SO_4 yields SSP, where the chemical composition and structure of the PK fibers are significantly altered and a high degree of disorder in the graphitic domains is developed (see Sections 3.2.1 and 3.3.2). This is witnessed by the decrease in d_{dom}, which for SSP reaches a value of ca. 1.5 nm. The pyrolysis processes applied on SSP to yield S300, S500 and S700 increase significantly d_{dom}. The higher T_p, the larger is d_{dom}:
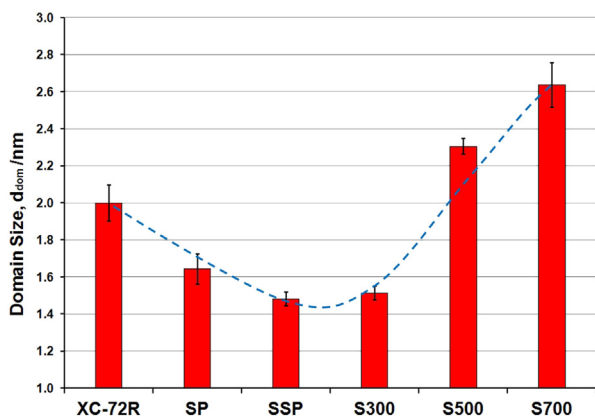

Fig. 4 — Size of the ordered domains d_{dom} of the support precursors and ST_p supports determined from the data reported in Fig. 3.

S300 < S500 < S700. This picture is coherent with a progressive increase in the degree of graphitization of the materials as T_p is raised, triggered by the removal of the volatile species based on heteroatoms (e.g., sulfur, oxygen and hydrogen; see Section 3.2.1) as the host medium undergoes reorganization processes. As a result, the concentration of structural defects decreases and the crystallinity of the ST_p support NPs rises (see Fig. 4).

3.3.4. Morphology studies

The morphology of SSP and of the S500 and S700 ST_p supports is investigated by HR-TEM; the resulting micrographs are shown in Fig. 5. The micrograph of SSP, shown in Fig. 5(a), demonstrates that PK fibers are bundled on the surface of XC-72R carbon NPs, giving so rise to the formation of a polymeric "nanoball". The micrographs of the ST_p supports (see Fig. 5(b) and (c)) show that: (a) S500 exhibits a very rough morphology, which is originated by the partial thermal degradation of the PK fibers grown on the surface of the "core" XC-72R carbon NPs (see Fig. 5(b)); (b) S700 is characterized by a more compact morphology in comparison with S500 (see Fig. 5(c)). This result is rationalized admitting that the PK fibers on the "shell" of S700 undergo aggregation and crystallization processes during the last pyrolysis step after the expulsion of the volatile species. Additional information on the morphology of the ST_p supports is determined by nitrogen physisorption studies (BET). The results are summarized in Table 4. The total surface area of the ST_p supports decreases in the order: S500 > S700 > XC-72R. This evidence is consistent with the morphology results of S500 and S700 obtained by HR-TEM (see Fig. 5(b) and (c)). The surface area of XC-72R carbon NPs is the smallest since this material consists of compact solid graphite NPs with an average diameter falling between ca. 30 and 50 nm [50]. The surface area determined by N_2 physisorption measurements consists of two contributions: (a) the external surface area; and (b) the area of the micropores embedded in the samples. The area of the micropores increases in the order: XC-72R < S700 < S500. The area of the micropores of XC-72R is the smallest since the surface roughness of the graphite NPs is very low. The higher area of the micropores observed in S500 suggests that at $T_p = 500\ °C$: (a) the elimination of the volatile species in the S300 ST_p support originates the rough and highly porous morphology shown in Fig. 5(b); and (b) T_p is low enough to prevent the reorganization of the pyrolyzed matrix. The latter phenomenon takes place for S700, which is obtained with $T_p = 700\ °C$. The surface area of the S700 micropores is lower in comparison with S500. The external surface area of the ST_p supports decreases in the order: XC-72R > S500 > S700. The decrease from S500 to S700 is consistent with a more compact morphology of S700 owing to host matrix reorganization processes upon pyrolysis reaction. In conclusion, the results of the investigations carried out by HR-TEM and nitrogen physisorption measurements are:

a) XC-72R (a typical "reference" support for PEMFC electrocatalysts [11,50] is characterized by the lowest surface area; the contribution of the micropores is the smallest (i.e., lower than ca 50%), while the external surface area is the largest of the three materials.
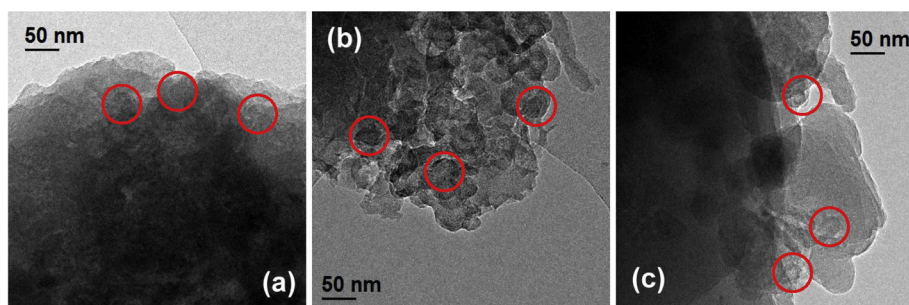
Fig. 5 – HR-TEM micrographs of: (a) SSP; (b) S500; and (c) S700. The red circles highlight a few of the primary XC-72R NPs. (For interpretation of the references to color in this figure legend, the reader is referred to the web version of this article.)

b) S500 shows a higher roughness; the surface area is mostly ascribed to the internal micropores, while the external surface area is significantly smaller in comparison with XC-72R. Therefore, the morphologies of XC-72R and S500 are completely different. S500 shows a relatively low number of distinct particles embedding a multitude of small internal cavities.

c) The morphology of S700, which is characterized by a smoother and more compact structure, is more similar to S500 than to XC-72R and exhibits the lowest external surface area and fewer internal cavities in comparison with S500.

3.4. Characterization of the electrocatalysts

3.4.1. HR-TGA analysis

The TG profiles of the electrocatalysts under inert and oxidizing atmospheres are shown in Figs. 6 and 7, respectively. The main figures of merit measured from the TGA profiles of the electrocatalysts shown in Figs. 6 and 7 are reported in Table 5. It is observed that the mass loss at $T = 500\,°C$ under an inert atmosphere: (a) decreases as both T_f and T_p are raised; (b) increases upon treatment with H_2O_2, and this effect is more pronounced for the electrocatalysts obtained at $T_f = 600\,°C$. The temperature of the main decomposition event determined under an oxidizing atmosphere (T_D): (a) for pristine PtNi-CN$_l$ T_f/ST_p electrocatalysts, increases as both T_f and T_p are raised; (b) increases upon treatment with H_2O_2; this event presents a larger extent for the electrocatalysts obtained at $T_f = 600\,°C$; and (c) in PtNi-CN$_l$ T_f/ST_p is revealed at higher temperatures with respect to the Pt/C reference. The intense degradation event revealed under oxidizing atmosphere at $400 < T < 500\,°C$ (Fig. 7) is attributed to the degradation of the electrocatalysts' matrix [29,31]. The intensity of the mass loss at $T = 500\,°C$ under inert atmosphere increases as T_D

decreases. Indeed, as the degree of graphitization increases, the concentration of volatile species based on heteroatoms which are eliminated from the CN "shell" matrix decreases (see Table 2). Consequently, the thermal stability of PtNi-CN$_l$ T_f/ST_p is improved both under inert and oxidizing atmosphere and the degree of graphitization of the CN "shell" matrix increases as T_f is raised, as discussed in Section 3.3.1. The morphology of the supports plays a crucial role in the modulation of the thermal stability of the samples; indeed, as T_p is increased the external surface area of ST_p supports determined by nitrogen physisorption measurements decreases (see Section 3.3.4. and Table 4). In PtNi-CN$_l$ T_f/ST_p a fraction of the CN "shell" matrix covers the external surface of the ST_p support NPs (I); the remaining fraction is embedded in their micropores (II). Under inert atmosphere it is expected that the thermal degradation products are more easily eliminated from CN domains (I) with respect to (II). As a result, at $T = 500\,°C$ the mass loss of electrocatalysts based on S700 is lower in comparison with that of the electrocatalysts including S500 ST_p "core" support. Under an oxidizing atmosphere, it is expected that the degradation of (I) domains occurs before (II) for analogous reasons. Therefore, T_D increases concurrently with T_p of the ST_p "core" support. The Pt/C reference, which is based on a XC-72R support, is characterized by the largest external surface area (see Table 4) and presents the lowest T_D (see Table 5). The treatment of PtNi-CN$_l$ T_f/ST_p with H_2O_2 facilitates the elimination of a significant fraction of the volatile species based on heteroatoms from the electrocatalysts, as discussed above in Section 3.2.2. Thus, the graphitization degree of the CN "shell" matrix and the thermal stability of the resulting electrocatalysts are significantly influenced by H_2O_2 treatment (see Table 5). The improved thermal stability of PtNi-CN$_l$ T_f/ST_p electrocatalysts is more pronounced for the systems obtained at $T_f = 900\,°C$. It is

Table 4 – Morphology parameters of the materials determined by nitrogen physisorption measurements.

Material	Surface area/$m^2\,g^{-1}$	External surface area/$m^2\,g^{-1}$	Area of the micropores/$m^2\,g^{-1}$	Volume of the micropores/$cm^3\,g^{-1}$
S500	452.8	70.7	382.1	0.196
S700	276.5	62.2	214.3	0.109
XC-72R	185.4	104.8	80.6	0.04

Surface area = External surface area + Area of the micropores.
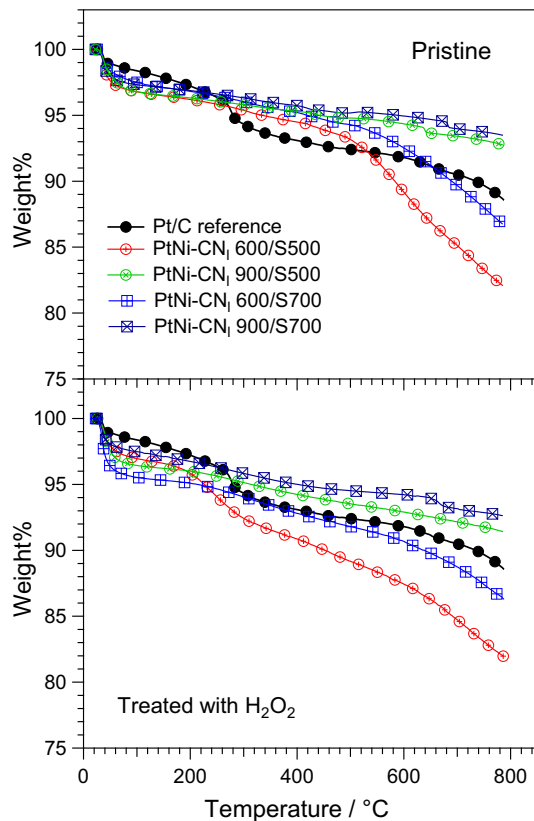
Fig. 6 — TG profiles under inert atmosphere of pristine (upper panel) and treated with H_2O_2 (lower panel) PtNi-CN$_l$ T_f/ST$_p$ electrocatalysts.
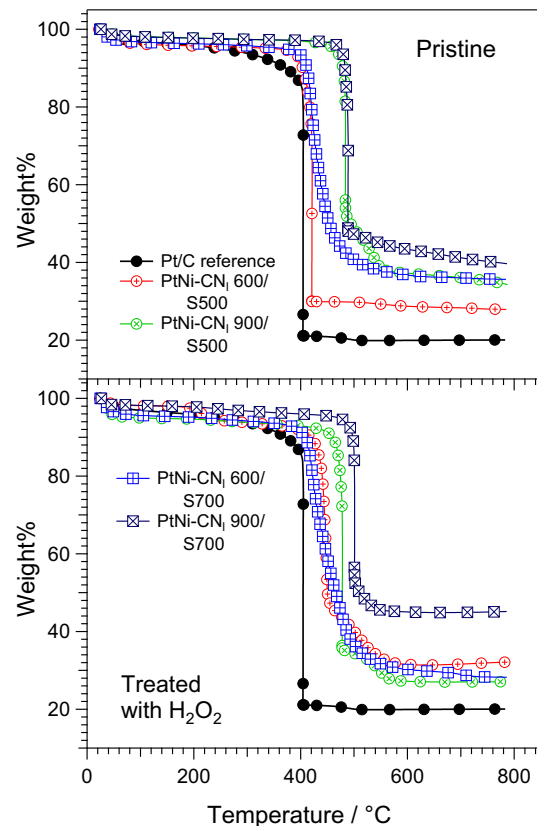

Fig. 7 — TG profiles under oxidizing atmosphere of pristine (upper panel) and treated with H_2O_2 (lower panel) PtNi-CN$_l$ T_f/ST$_p$ electrocatalysts.

hypothesized that the increase in the mass loss at $T = 500\ °C$ occurring under an inert atmosphere upon treatment with H_2O_2 (see Table 5) takes place owing to the oxidation of surface functional groups present on the surface of the electrocatalysts. As a result, new pathways are created from the micropores to the external surface of the electrocatalysts. The outcome is an increase of the concentration of surface functional groups, which are easily eliminated giving so rise to a higher mass loss at $T = 500\ °C$ under an inert atmosphere. This phenomenon is more evident for the electrocatalysts prepared at $T_f = 600\ °C$, with a lower degree of graphitization in the CN "shell" matrix covering the external surface of the ST$_p$ "core" supports. In these conditions, the oxidative attack of H_2O_2 is more effective and consequently the elimination of volatile degradation products is facilitated.

3.4.2. Tests in a single-cell configuration

The polarization and power curves of the MEAs mounting the proposed PtNi-CN$_l$ T_f/ST$_p$ electrocatalysts on the cathodic electrodes are shown in Figs. 8 and 9. The pristine electrocatalysts yielding the best fuel cell performance are PtNi-CN$_l$ 600/S700 and PtNi-CN$_l$ 900/S500 (Fig. 8), while PtNi-CN$_l$ 900/S700 and PtNi-CN$_l$ 600/S500 present a reduced activity. To analyze these results we should consider that an efficient electrocatalyst requires: (a) a support with a high electron conductivity; and (b) active sites distributed on a large area and with a high turnover frequency at overpotentials as

small as possible [4,11]. These requirements play a crucial role in the materials here proposed. Indeed, the treatment with H_2O_2 does not affect significantly the Pt/Ni atomic ratio (see Table 2). Thus, in first approximation it can be expected that at any given ORR overpotential the intrinsic turnover frequency of a pristine electrocatalyst and of the corresponding sample treated with H_2O_2 are very close. Furthermore, the graphitization degree of the ST$_p$ "core" supports increases in the order: S500 < S700, as discussed in Sections 3.2 and 3.3. Thus, the electron conductivity of S700 is higher

Table 5 — TGA figures of merit of the PtNi-CN$_l$ T_f/ST$_p$ electrocatalysts.

Electrocatalyst	ML@500 °C[a]/wt%		T_D[b]/°C	
	Pristine	(w)[c]	Pristine	(w)[c]
PtNi-CN$_l$ 600/S500	6.8	10.8	421	445
PtNi-CN$_l$ 900/S500	5.3	6.5	484	478
PtNi-CN$_l$ 600/S700	5.7	8.2	433	445
PtNi-CN$_l$ 900/S700	4.8	5.5	489	501
Pt/C reference	7.6		404	

[a] Mass loss at 500 °C determined under an inert atmosphere.
[b] T_D is the temperature of main decomposition event obtained under an oxidizing atmosphere.
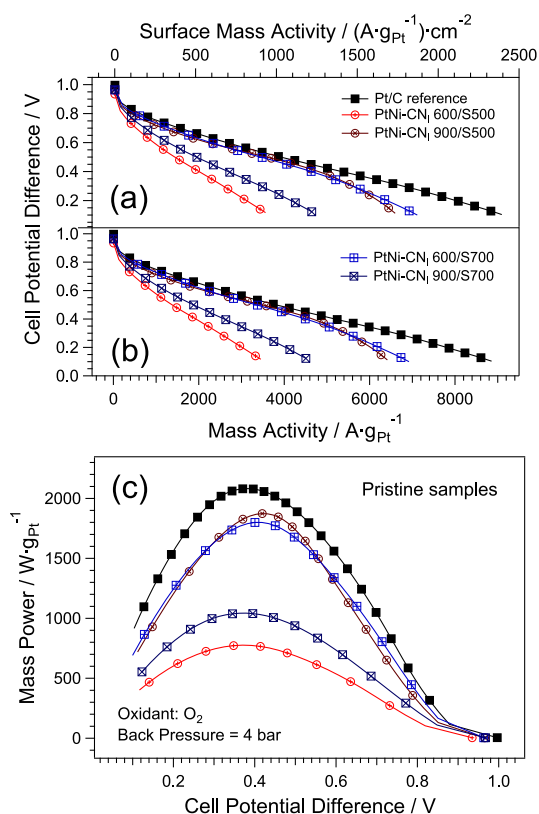[c] (w) = Treated with H_2O_2.

Fig. 8 – Polarization curves of pristine PtNi-CN$_l$ T_f/ST$_p$ electrocatalysts normalized with respect to: (a) active area of the electrodes and Pt mass present on the cathodic electrode; (b) Pt mass present on the cathodic electrode. (c) Electrical power profiles of prepared MEAs normalized on Pt mass present on the cathodic electrode. Tests are carried out with a 5 cm^2 single cell operating with pure H$_2$ on anode and pure O$_2$ at cathode. H$_2$ and O$_2$ flow rates are 800 and 500 sccm, respectively; $T_{anode/cell/cathode}$ = 84/85/84 °C; RH = 100%; reagents back pressure = 4 bar.

Fig. 9 – Polarization curves of PtNi-CN$_l$ T_f/ST$_p$(w) electrocatalysts normalized with respect to: (a) active area of the electrodes and Pt mass present on the cathodic electrode; (b) Pt mass present on the cathodic electrode. (c) Electrical power profiles of prepared MEAs normalized on Pt mass present on the cathodic electrode. Tests are carried as described in the caption of Fig. 8.

than that of S500. It was reported that in CN-based electrocatalyst the single fuel cell performance decreases as T_f is raised [30]. This evidence is interpreted considering that at T_f = 900 °C the PtNi$_x$ alloy NPs generally undergo growth/aggregation processes, which act to reduce significantly the active surface area of the electrocatalyst [30]. It is supposed that the good fuel cell performance of PtNi-CN$_l$ 600/S700 is likely associated to the good electron conductivity of S700 ST$_p$ "core" support and to the presence of PtNi$_x$ alloy NPs obtained at T_f = 600 °C with a lower size. In PtNi-CN$_l$ 900/S700, a significantly lower fuel cell performance is revealed, which indicates that in this case the active sites are buried in the CN "shell" matrix originated at T_f = 900 °C. The promising performance in single fuel cell of PtNi-CN$_l$ 900/S500 is associated to the stabilizing effect of the chemical composition of the CN "shell" matrix and to the porous morphology of the S500 ST$_p$ "core" support. The latter actually limits the growth/aggregation process of the PtNi$_x$ alloy NPs, where the active sites for the ORR are found [32]. The treatment at T_f = 900 °C is also assumed to improve the graphitization degree of the
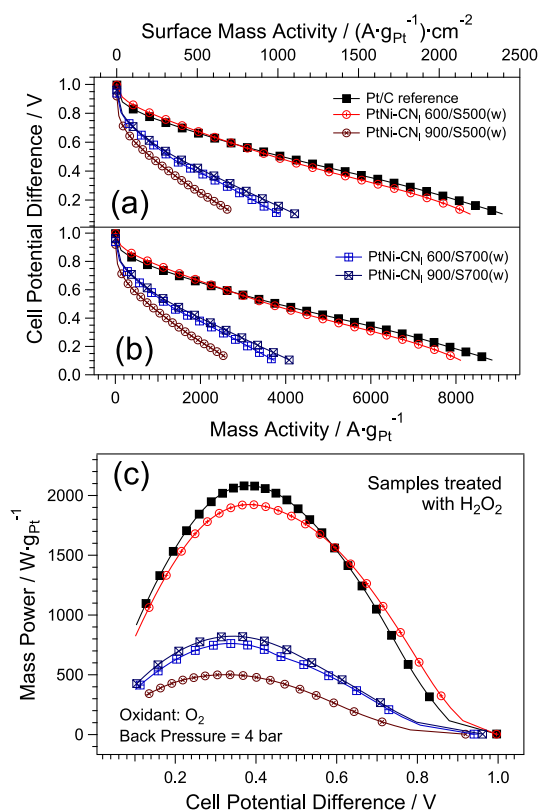
S500 ST$_p$ "core" support, thus increasing the electron conductivity. In the case of PtNi-CN$_l$ 600/S500 the PtNi$_x$ alloy NPs are probably small; however, the electron conductivity of the ST$_p$ "core" support is most likely poor, compromising the fuel cell performance of the electrocatalyst. Fig. 10 compares the
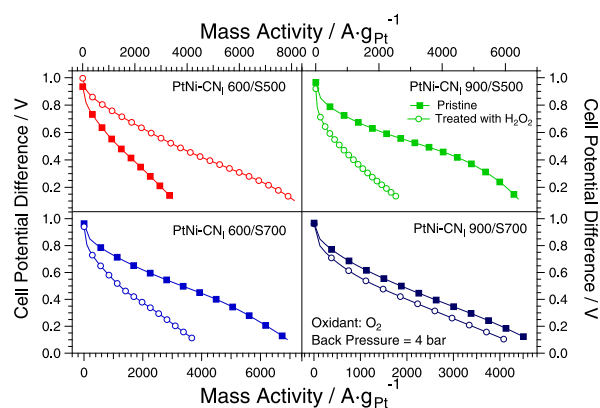

Fig. 10 – Comparison of the fuel cell performance of electrocatalysts with and without the treatment with H$_2$O$_2$. The polarization curves are collected as described in the caption of Fig. 8.

fuel cell performance of the electrocatalysts with and without the treatment with H_2O_2. It should be noticed that the fuel cell performance of PtNi-CN$_l$ 600/S700(w), PtNi-CN$_l$ 900/S500(w) and PtNi-CN$_l$ 900/S700(w) is inferior in comparison with the corresponding pristine electrocatalyst. The exception is PtNi-CN$_l$ 600/S500(w), whose fuel cell performance is significantly improved in comparison with PtNi-CN$_l$ 600/S500 and is very similar to the Pt/C reference. At mass activities lower than ca. 2700 A g_{Pt}^{-1}, the cell voltage of PtNi-CN$_l$ 600/S500(w) is larger by up to ca. 20–25 mV in comparison with the Pt/C reference (see Fig. 9). The behavior of the electrocatalysts upon treatment in H_2O_2 is likely correlated to the mass transport of reactants and products in the cathodic electrocatalytic layers [51]. The MEAs fabricated with the prepared electrocatalysts are tested: (a) at different values of back pressure, using as the oxidant either air or pure oxygen; (b) keeping constant the other fuel cell operating parameters; and (c) analyzing MEA performance both in low-current and high-current regimes. In the low-current regime (i.e., at 50 A g_{Pt}^{-1}, corresponding to ca. 5.4 mA cm^{-2}) very little water is produced at the cathodic active sites upon fuel cell operation and the ohmic drops are very small and can be neglected. Thus, in this condition the performance of the cathode is mainly controlled by the ORR kinetics and by the diffusion of oxygen to the active sites. Table 6 includes the cell voltage at 50 A g_{Pt}^{-1} under various operating conditions. It is observed that in general the values of V@50 A g_{Pt}^{-1} decrease significantly upon treatment with H_2O_2, using both air and pure O_2 as the oxidant, and at back pressure values of both 4 and 1 bar. The only exception is PtNi-CN$_l$ 600/S500(w). Using pure O_2 at a back pressure of 4 bar as the oxidant, this electrocatalyst shows a V@50 A g_{Pt}^{-1}: (a) higher than that of the corresponding pristine electrocatalyst; and (b) slightly higher than the Pt/C reference. This latter evidence is consistent with the enhanced ORR performance of PtNi$_x$ alloy NPs in comparison with the pure Pt NPs of the Pt/C reference [30,32]. Table 6 reports the values of two figures of merit, Δ_4 and Δ_1, which are measured at an oxidant back pressure of either 4 or 1 bar, respectively, as described in the caption of Table 6. Large values of Δ_4 and Δ_1 witness that the performance of a fuel cell

increases significantly as the oxidant is changed from air to pure O_2. This is a direct evidence that the O_2 transport to the active sites is hindered by electrocatalyst morphology, irrespectively of the ORR kinetics. The inspection of Table 6 indicates clearly that the values of both Δ_4 and Δ_1: (a) increase significantly upon treatment with H_2O_2; (b) increase from PtNi-CN$_l$ T$_f$/S500 to PtNi-CN$_l$ T$_f$/S700; and (c) are quite similar for the proposed electrocatalysts and the Pt/C reference. Results suggest that: (a) after treatment with H_2O_2, the active sites are buried more deeply in the electrocatalytic layers, and are less accessible by O_2 reactant molecules; no such effect is revealed for PtNi-CN$_l$ 900/S700; (b) the surface area of the support plays a crucial role in the oxygen transport towards the ORR active sites (see Table 4); and (c) the mechanism of O_2 transport towards the active sites of the proposed electrocatalysts and of the Pt/C reference is similar. The effect of the transport of reagents and products in the cathodic electrocatalytic layers is also evaluated in the high-current regime, by two additional figures of merit, Ψ_4 and Ψ_1 (Table 7), which are defined and evaluated for each electrocatalyst. On the basis of the maximum values of the mass power curves, a significant production of water is expected at the cathodic ORR active sites upon fuel cell operation. This water may flood the active sites of the electrocatalysts, thus blocking the incoming O_2 molecules and limiting the fuel cell performance. Flooding is easier if the active sites are embedded inside the micropores of the ST$_p$ "core" support, since in these conditions the removal of water obtained as the product of fuel cell operation is more difficult. This "blocking effect" is expected to become more relevant as the partial pressure of O_2 in the cathodic compartment is lowered, e.g., switching from pure O_2 to air as the oxidant [52]. It should be pointed out that the transport of O_2 to the ORR active sites is still expected to play an important role in the fuel cell performance in the high-current regime. In summary, a high value of Ψ_i (i = 1,4) indicates that the fuel cell performance depends strongly on the partial pressure of O_2, including the contributions arising from both: (a) the transport of oxygen to the active sites; and (b) the removal of water obtained as the final product of the ORR during fuel cell

Table 6 – Figures of merit of fuel cell performance in the low-current regime.

Oxidant back pressure	4 bar			1 bar		
Cathode electrocatalysts	O_2[a] V@50 A g_{Pt}^{-1}/mV	Air[a] V@50 A g_{Pt}^{-1}/mV	Δ_4[b] mV	O_2[a] V@50 A g_{Pt}^{-1}/mV	Air[a] V@50 A g_{Pt}^{-1}/mV	Δ_1[c] mV
PtNi-CN$_l$ 600/S500	835	802	33	811	771	40
PtNi-CN$_l$ 600/S500(w)	906	846	60	878	830	48
PtNi-CN$_l$ 900/S500	873	836	37	819	777	42
PtNi-CN$_l$ 900/S500(w)	756	691	65	717	641	76
PtNi-CN$_l$ 600/S700	885	837	48	855	821	34
PtNi-CN$_l$ 600/S700(w)	806	735	71	733	654	79
PtNi-CN$_l$ 900/S700	860	795	65	789	728	61
PtNi-CN$_l$ 900/S700(w)	822	759	63	776	705	71
Pt/C reference	904	857	47	872	820	52

[a] The polarization curves used to obtain these results are displayed in Supplementary Data.
[b] Δ_4 = V@50 A g_{Pt}^{-1} [O_2, 4 bar] – V@50 A g_{Pt}^{-1} [Air, 4 bar].
[c] Δ_1 = V@50 A g_{Pt}^{-1} [O_2, 1 bar] – V@50 A g_{Pt}^{-1} [Air, 1 bar].

Table 7 – Figures of merit for the mass transport phenomena in cathodic electrocatalytic layers in the high-current regime.

Cathode electrocatalysts	Ψ_4[a,c]	Ψ_1[b,c]
PtNi-CN$_l$ 600/S500	1.98	2.02
PtNi-CN$_l$ 600/S500(w)	2.77	2.35
PtNi-CN$_l$ 900/S500	2.16	2.17
PtNi-CN$_l$ 900/S500(w)	2.20	1.93
PtNi-CN$_l$ 600/S700	1.62	1.39
PtNi-CN$_l$ 600/S700(w)	1.85	1.78
PtNi-CN$_l$ 900/S700	1.68	1.94
PtNi-CN$_l$ 900/S700(w)	1.80	2.15
Pt/C reference	1.19	1.25

[a] Ψ_4 = Maximum mass power [O_2, 4 bar]/Maximum mass power [Air, 4 bar].
[b] Ψ_1 = Maximum mass power [O_2, 1 bar]/Maximum mass power [Air, 1 bar].
[c] The polarization curves used to evaluate Ψ_4 and Ψ_1 are displayed in Supplementary data.

operation. It can be admitted that the study of the fuel cell performance in the low-current and high-current operating regimes yields complementary information. (1) In the low-current regime, the transport of oxygen in the closest proximity of the active sites is investigated. (2) In the high-current regime, it is possible to obtain insight on the influence of the morphology of the electrocatalysts at larger scales on the fuel cell performance. Information (1) and (2) may be correlated respectively to the overall surface area of the support and the area of the micropores obtained by nitrogen physisorption experiments (see Table 4). The inspection of Table 7 highlights that the values of Ψ_4 and Ψ_1: (a) increase upon treatment with H_2O_2; (b) increase in the order: Pt/C reference $\ll$ PtNi-CN$_l$ T_f/S700 < PtNi-CN$_l$ T_f/S500. Results suggest that: (a) after the treatment with H_2O_2, the mass transport of reagents and products to/from the active sites is more difficult, probably because most of the active sites are located in the micropores of the ST$_p$ "core" supports; (b) the removal of water product is more difficult in those electrocatalysts based on supports featuring a larger area in the micropores (see Table 4). The results shown in Tables 6 and 7 and discussed above demonstrate (see Fig. 10) that the performance of PtNi-CN$_l$ 600/S700(w) is significantly reduced in comparison with PtNi-CN$_l$ 600/S700 since the treatment of this system with H_2O_2 removes the PtNi$_x$ alloy NPs which are more easily accessible to O_2 molecules; the surviving PtNi$_x$ alloy NPs are those which were originally deeply embedded in the micropores of the ST$_p$ "core" support. This interpretation is corroborated by the increase in Δ_1, Δ_4, Ψ_1 and Ψ_4 and in the decrease of the concentration of metals in the chemical composition of pristine electrocatalysts upon treatment with H_2O_2 (see Tables 2, 6 and 7). The decrease in the fuel cell performance of PtNi-CN$_l$ 900/S700 after treatment in H_2O_2 is small (see Fig. 10), thus witnessing that the original morphology of the electrocatalyst is likely characterized by large PtNi$_x$ alloy NPs which are deeply buried in the micropores of the ST$_p$ "core" support. The treatment with H_2O_2 of this system influences slightly the morphology of the electrocatalyst. Indeed, the pronounced graphitization of both

the S700 ST$_p$ "core" support and of its electrocatalyst CN "shell" matrix (see Sections 3.2, 3.3 and 3.4.1) is expected to improve the binding ability of the PtNi$_x$ alloy NPs bearing the ORR active sites. Large values of Δ_1, Δ_4, Ψ_1 and Ψ_4 are diagnostic of the electrocatalyst morphologies. The decrease in fuel cell performance from PtNi-CN$_l$ 900/S500 to PtNi-CN$_l$ 900/S500(w) is expected to occur owing to the same phenomena described above for PtNi-CN$_l$ 600/S700, i.e. the elimination of the most easily accessible PtNi$_x$ alloy NPs upon treatment with H_2O_2. This hypothesis is consistent with the similar trends observed in the evolution of Δ_1 and Δ_4 upon treatment with H_2O_2 in both PtNi-CN$_l$ 600/S700 and PtNi-CN$_l$ 900/S500 (see Table 6). It should be observed that, with respect to PtNi-CN$_l$ 600/S700, the values of Ψ_1 and Ψ_4 in PtNi-CN$_l$ 900/S500 are larger, and are not significantly influenced by treatment with H_2O_2. Thus, it can be concluded that: (a) PtNi-CN$_l$ 600/S700 presents a more compact morphology than PtNi-CN$_l$ 900/S500, consistently with a lower surface area revealed for the micropores of the S700 ST$_p$ "core" support in comparison with S500; and (b) the morphology of PtNi-CN$_l$ 900/S500 at the micropore level is not affected by H_2O_2 treatment as expected on the basis of a more pronounced graphitization degree at T_f = 900 °C (see Sections 3.2, 3.3 and 3.4.1) of the support matrix, i.e. the S500 ST$_p$ "core" support covered by the CN "shell" matrix. The significant increase in fuel cell performance from PtNi-CN$_l$ 600/S500 to PtNi-CN$_l$ 600/S500(w) is accompanied by a remarkable increase in Δ_1, Δ_4, Ψ_1 and Ψ_4. The increase is particularly evident for Ψ_1 and Ψ_4 (see Table 7). The treatment of the pristine electrocatalyst with H_2O_2 gives rise to the following phenomena: (a) a portion of the support matrix which is less graphitized is removed through oxidation by H_2O_2. Accordingly, new micropores are generated in the material and Ψ_1, Ψ_4 and the electron conductivity value of the support matrix rise; (b) some PtNi$_x$ alloy NPs are eliminated, leading to the observed decrease in the concentration of Pt and Ni in PtNi-CN$_l$ 600/S500(w) (see Table 2); and (c) a fraction of PtNi$_x$ alloy NPs originally buried deeply within the bulk support micropores becomes accessible for the ORR as the microporosity of the support matrix is improved. The PtNi$_x$ alloy NPs are difficult to remove when they are coordinated by the nitrogen atoms included in the CN "shell" matrix of the PtNi-CN$_l$ 600/S500(w) electrocatalyst; in this way, PtNi$_x$ alloy NPs are stabilized by binding processes on nitrogen-based "coordination nests" [44]. It is pointed out that these are only a fraction of the active sites present on the surface of PtNi$_x$ alloy NPs accessible to O_2, thus raising the values of Δ_1 and Δ_4.

4.   Conclusions

In this report two new ST$_p$ supports, S500 and S700, are prepared by sulfonation and pyrolysis of a support precursor (SP) consisting of XC-72R carbon NPs embedded in a "ball" of PK fibers. The detailed studies carried out on the support precursors and ST$_p$ "core" supports show that: (a) a successful incorporation of sulfur atoms in the chemical composition of the materials occurs; (b) the graphitization of SP becomes more evident as T_p is raised; and (c) a complex interplay takes place between the parameters of the

preparation processes and the morphology of the ST_p "core" support NPs. The latter is different in comparison to that of the carbon black nanoparticles commercially used as support in state-of-the-art fuel cell electrocatalysts. S500 and S700 are used in the synthesis of new "core—shell" PtNi-CN$_l$ T_f/S500 and PtNi-CN$_l$ T_f/S700 electrocatalysts. The latter are prepared by a pyrolysis process at T_f = 600 or 900 °C of a precursor obtained by supporting a Z-IOPE plastic material on either S500 or S700 ST_p "core" supports. The effect of H_2O_2 treatments of the proposed electrocatalysts is investigated. The prepared electrocatalysts undergo extensive chemical and thermal characterization and are finally adopted as the cathodic electrocatalysts in the fabrication of MEAs tested in single-cell configuration in operative conditions at different partial pressures of O_2. A complex interplay is revealed between the fuel cell performance and the chemical composition, the graphitization degree, and the morphology of both the ST_p "core" supports and the final "core—shell" electrocatalysts. In particular, it is observed that the best fuel cell performance for pristine electrocatalysts is obtained for PtNi-CN$_l$ 600/S700 and PtNi-CN$_l$ 900/S500. These materials show: (a) a high electrical conductivity; and (b) PtNi$_x$ alloy NPs bearing the ORR active sites characterized by a relatively large accessible surface area. The treatment of the electrocatalysts with H_2O_2 compromises the fuel cell performance because of the elimination of a fraction of PtNi$_x$ alloy NPs. PtNi-CN$_l$ 600/S500 is an exception: indeed, its performance improves significantly upon treatment with H_2O_2, reaching essentially the same level of the Pt/C reference as pure O_2 at a back pressure of 4 bar is used as the oxidant. This unexpected behavior is justified considering that upon treatment with H_2O_2 the support matrix of PtNi-CN$_l$ 600/S500 becomes more electrically conductive and microporous; in this way, additional PtNi$_x$ alloy NPs bearing ORR active sites are made accessible. Finally, it should be noticed that the nitrogen atoms of the CN "shell" matrix of PtNi-CN$_l$ 600/S500 coordinate the PtNi$_x$ alloy NPs, binding them to the PtNi$_x$-CN "shell" and partially inhibiting their removal upon treatment with H_2O_2. Indeed, the N-based functional groups of the CN "shell" matrix play a crucial role in stabilizing and activating the electrocatalysts. Taken together, in this report new ST_p supports are proposed based on precursors covered by PK fibers, and the most crucial preparation parameters that must be controlled to devise new and active ORR electrocatalysts including those ST_p supports are described. These electrocatalysts result very promising, even if further studies are necessary to better modulate the complex interplay between the chemical composition, morphology and electrochemical activity, with the ultimate aim to improve their fuel cell performance.

Acknowledgments

Appendix A. Supplementary data

Supplementary data related to this article can be found at http://dx.doi.org/10.1016/j.ijhydene.2013.08.054.

REFERENCES

[1] O'Hayre R, Cha SW, Colella W, Printz FB. Fuel cell fundamentals. Hoboken, NJ: John Wiley & Sons; 2006.

[2] Srinivasan S. Fuel cells — from fundamentals to applications. New York: Springer Science; 2006.

[3] Di Noto V, Zawodzinski TA, Herring AM, Giffin GA, Negro E, Lavina S. Polymer electrolytes for a hydrogen economy. Int J Hydrogen Energy 2012;37:6120—31.

[4] Spiegel CS. Designing and building fuel cells. New York: McGraw-Hill; 2007.

[5] Vielstich W. In: Vielstich W, Lamm A, Gasteiger HA, editors. Handbook of fuel cells: fundamentals technology and applications. Chichester: John Wiley & Sons; 2003. p. 26—30.

[6] Konrad G, Sommer M, Loschko B, Schell A, Docter A. In: Vielstich W, Lamm A, Gasteiger HA, editors. Handbook of fuel cells: fundamentals, technology, and applications. Hoboken, NJ: John Wiley & Sons; 2003. p. 693—771.

[7] Deabate S, Gebel G, Huguet P, Morin A, Pourcelly G. In situ and operando determination of the water content distribution in proton conducting membranes for fuel cells: a critical review. Energy Environ Sci 2012;5:8824—47.

[8] Morozan A, Jousselme B, Palacin S. Low-platinum and platinum-free catalysts for the oxygen reduction reaction at fuel cell cathodes. Energy Environ Sci 2011;4:1238—54.

[9] Antolini E. Formation of carbon-supported PtM alloys for low temperature fuel cells: a review. Mater Chem Phys 2003;78:563—7.

[10] Watanabe M, Tryk DA, Wakisaka M, Yano H, Uchida H. Overview of recent developments in oxygen reduction electrocatalysis. Electrochim Acta 2012;84:187—201.

[11] Gasteiger HA, Kocha SS, Sompalli B, Wagner FT. Activity benchmarks and requirements for Pt, Pt-alloy, and non-Pt oxygen reduction catalysts for PEMFCs. Appl Catal B Environ 2005;56:9—35.

[12] Huang S, Ganesan P, Popov BN. Electrocatalytic activity and stability of titania-supported platinum-palladium electrocatalysts for polymer electrolyte membrane fuel cell. ACS Catal 2012;2:825—31.

[13] Xu Z, Zhang H, Zhong H, Lu Q, Wang Y, Su D. Effect of particle size on the activity and durability of the Pt/C electrocatalyst for proton exchange membrane fuel cells. Appl Catal B Environ 2012;111—112:264—70.

[14] Borup R, Meyers J, Pivovar B, Kim YS, Mukundan R, Garland N, et al. Scientific aspects of polymer electrolyte fuel cell durability and degradation. Chem Rev 2007;107:3904—51.

[15] Di Noto V, Negro E, Lavina S, Gross S, Pace G. Pd—Co carbon-nitride electrocatalysts for polymer electrolyte fuel cells. Electrochim Acta 2007;53:1604—17.

[16] Drillet J, Ee A, Friedemann J, Kötz R, Schnyder B, Schmidt VM. Oxygen reduction at Pt and Pt$_{70}$Ni$_{30}$ in H_2SO_4/CH_3OH solution. Electrochim Acta 2002;47:1983—8.

[17] Toda T, Igarashi H, Uchida H, Watanabe M. Enhancement of the electroreduction of oxygen on Pt alloys with Fe, Ni, and Co. J Electrochem Soc 1999;146:3750—6.

[18] Yang H, Coutanceau C, Léger J, Alonso-Vante N, Lamy C. Methanol tolerant oxygen reduction on carbon-supported Pt—Ni alloy nanoparticles. J Electroanal Chem 2005;576:305—13.

[19] Greeley J, Stephens IEL, Bondarenko AS, Johansson TP, Hansen HA, Jaramillo TF, et al. Alloys of platinum and early transition metals as oxygen reduction electrocatalysts. Nat Chem 2009;1:552–6.

[20] Di Noto V, Negro E, Gliubizzi R, Gross S, Maccato C, Pace G. Pt and Ni carbon nitride electrocatalysts for the oxygen reduction reaction. J Electrochem Soc 2007;154:B745–56.

[21] Salvatore Aricó A, Stassi A, Gatto I, Monforte G, Passalacqua E, Antonucci V. Surface properties of Pt and PtCo electrocatalysts and their influence on the performance and degradation of high-temperature polymer electrolyte fuel cells. J Phys Chem C 2010;114:15823–36.

[22] Stassi A, Gatto I, Monforte G, Passalacqua E, Antonucci V, Aricò AS. Investigation of carbon supported Pt and PtCo electrocatalysts by low-energy ion scattering and X-ray photoelectron spectroscopy: influence of the surface characteristics on performance and degradation. ECS Trans 2011;35:83–91.

[23] Teliska M, Murthi VS, Mukerjee S, Ramaker DE. Correlation of water activation, surface properties, and oxygen reduction reactivity of supported Pt–M/C bimetallic electrocatalysts using XAS. J Electrochem Soc 2005;152:A2159–69.

[24] Qian Y, Wen W, Adcock PA, Jiang Z, Hakim N, Saha MS, et al. PtM/C catalyst prepared using reverse micelle method for oxygen reduction reaction in PEM fuel cells. J Phys Chem C 2008;112:1146–57.

[25] Roy SC, Harding AW, Russell AE, Thomas KM. Spectroelectrochemical study of the role played by carbon functionality in fuel cell electrodes. J Electrochem Soc 1997;144:2323–8.

[26] Yu S, Lou Q, Han K, Wang Z, Zhu H. Synthesis and electrocatalytic performance of MWCNT-supported Ag@Pt core-shell nanoparticles for ORR. Int J Hydrogen Energy 2012;37:13365–70.

[27] Vinayan BP, Nagar R, Rajalakshmi N, Ramaprabhu S. Novel platinum–cobalt alloy nanoparticles dispersed on nitrogen-doped graphene as a cathode electrocatalyst for PEMFC applications. Adv Funct Mater 2012;22:3519–26.

[28] Di Noto V, Negro E. Patent PCT/IT2009/000278.

[29] Di Noto V, Negro E. Development of nano-electrocatalysts based on carbon nitride supports for the ORR processes in PEM fuel cells. Electrochim Acta 2010;55:7564–74.

[30] Di Noto V, Negro E. Pt–Fe and Pt–Ni carbon nitride-based "core-shell" ORR electrocatalysts for polymer electrolyte membrane fuel cells. Fuel Cells 2010;10:234–44.

[31] Di Noto V, Negro E, Polizzi S, Riello P, Atanassov P. Preparation, characterization and single-cell performance of a new class of Pd–carbon nitride electrocatalysts for oxygen reduction reaction in PEMFCs. Appl Catal B Environ 2012;111–112:185–99.

[32] Di Noto V, Negro E, Polizzi S, Agresti F, Giffin GA. Synthesis–structure–morphology interplay of bimetallic "core-shell" carbon nitride nano-electrocatalysts. ChemSusChem 2012;5:2451–9.

[33] Di Noto V, Negro E, Lavina S, Boaretto N, Piga M. Platinum-free carbon nitride electrocatalysts for PEMFCs based on Pd, Co and Ni: effect of nitrogen on the structure and electrochemical performance. ECS Trans 2008;16:123–37.

[34] Di Noto V, Piga M, Giffin GA, Schuster M, Cavinato G, Toniolo L, et al. New sulfonated poly(p -phenylenesulfone)/poly(1-oxotrimethylene) nanocomposite proton-conducting membranes for PEMFCs. Chem Mater 2011;23:4452–8.

[35] Benetollo F, Bertani R, Bombieri G, Toniolo L. Synthesis, characterization and X-ray structure of [Pd(dppp)(H$_2$O)(TsO)] [TsO] (dppp = 1,3-bis(diphenylphosphino)propane; TsO = p-CH$_3$C$_6$H$_4$SO$_3$), a catalytic species in COC$_2$H$_4$ copolymerization. Inorg Chim Acta 1995;233:5–9.

[36] Fabrello A, Vavasori A, Dall'Acqua F, Toniolo L. Influence of the reaction conditions on the productivity and on the molecular weight of the polyketone obtained by the CO-ethene copolymerisation catalysed by [Pd(TsO)(H$_2$O)(dppp)](TsO) in MeOH. J Mol Catal A Chem 2007;276:211–8.

[37] Di Noto V, Negro E. A new Pt–Rh carbon nitride electrocatalyst for the oxygen reduction reaction in polymer electrolyte membrane fuel cells: synthesis, characterization and single-cell performance. J Power Sources 2010;195:638–48.

[38] Di Noto V, Negro E, Gliubizzi R, Lavina S, Pace G, Gross S, et al. A Pt–Fe carbon nitride nano-electrocatalyst for polymer electrolyte membrane fuel cells and direct-methanol fuel cells: synthesis, characterization, and electrochemical studies. Adv Funct Mater 2007;17:3626–38.

[39] Kocha SS. In: Vielstich W, Lamm A, Gasteiger HA, editors. Handbook of fuel cells: fundamentals technology and applications. Chichester: John Wiley & Sons; 2003. p. 538–65.

[40] Di Noto V, Boaretto N, Negro E, Pace G. New inorganic–organic proton conducting membranes based on Nafion and hydrophobic fluoroalkylated silica nanoparticles. J Power Sources 2010;195:7734–42.

[41] Di Noto V. A novel polymer electrolyte based on oligo(ethylene glycol) 600, K$_2$PdCl$_4$, and K$_3$Fe(CN)$_6$. J Mater Res 1997;12:3393–403.

[42] Di Noto V, Vittadello M, Lavina S, Biscazzo S, Fauri M. The first lithium zeolitic inorganic–organic polymer electrolyte based on PEG600, Li$_2$PdCl$_4$ and Li$_3$Fe(CN)$_6$: part I, synthesis and vibrational studies. Electrochim Acta 2003;48:2047–58.

[43] Di Noto V, Vittadello M, Greenbaum SG, Suarez S, Kano K, Furukawa T. A new class of lithium hybrid gel electrolyte systems. J Phys Chem B 2004;108:18832–44.

[44] Di Noto V, Negro E, Vezzù K, Toniolo L, Pace G. Interplay between structural and electrochemical properties of Pt–Rh carbon nitride electrocatalysts for the oxygen reduction reaction. Electrochim Acta 2011;57:257–69.

[45] Lin-Vien D, Colthup NB, Fateley WG, Grasselli JG. The handbook of infrared and Raman characteristic frequencies of organic molecules. New York: Academic Press, Inc.; 1991.

[46] Drent E, Van Broekhoven JAM, Doyle MJ. Efficient palladium catalysts for the copolymerization of carbon monoxide with olefins to produce perfectly alternating polyketones. J Organomet Chem 1991;417:235–51.

[47] Rastoltseva EV, Bataev VA, Abramenkov AV, Pupyshev VI, Godunov IA. Structure and conformational dynamics of the dicyclopropyl ketone in the ground electronic state. J Mol Struct THEOCHEM 2010;939:14–21.

[48] Tuinstra F, Koenig JL. Raman spectrum of graphite. J Chem Phys 1970;53:1126–30.

[49] Sadezky A, Muckenhuber H, Grothe H, Niessner R, Pöschl U. Raman microspectroscopy of soot and related carbonaceous materials: spectral analysis and structural information. Carbon 2005;43:1731–42.

[50] Senthil Kumar SM, Soler Herrero J, Irusta S, Scott K. The effect of pretreatment of Vulcan XC-72R carbon on morphology and electrochemical oxygen reduction kinetics of supported Pd nano-particle in acidic electrolyte. J Electroanal Chem 2010;647:211–2.

[51] Chaparro AM, Ferreira-Aparicio P, Folgado MA, Martín AJ, Daza L. Catalyst layers for proton exchange membrane fuel cells prepared by electrospray deposition on Nafion membrane. J Power Sources 2011;196:4200–8.

[52] Prasanna M, Ha HY, Cho EA, Hong S-, Oh I-. Investigation of oxygen gain in polymer electrolyte membrane fuel cells. J Power Sources 2004;137:1–8.

[53] Kolev T. Vibrational assignment of in- and out-of-plane modes of some aromatic and arylaliphatic ketones. J Mol Struct 1995;249:381–4.